

Constraints on redshifts of blazars from extragalactic background light attenuation using *Fermi*-LAT data

Alberto Domínguez,¹* María Láinez,¹† Vaidehi S. Paliya,²‡ Nuria Álvarez-Crespo,¹ Marco Ajello,³ Justin Finke,⁴ Mireia Nievas-Rosillo,^{5,6} Jose Luis Contreras,¹ Abhishek Desai⁷

¹*IPARCOS and Department of EMFTEL, Universidad Complutense de Madrid, E-28040 Madrid, Spain*

²*Inter-University Centre for Astronomy and Astrophysics (IUCAA), SPPU Campus, 411007, Pune, India*

³*Department of Physics and Astronomy, Clemson University, Kinard Lab of Physics, Clemson, SC 29634-0978, US*

⁴*U.S. Naval Research Laboratory, Code 7653, 4555 Overlook Avenue SW, Washington, DC 20375-5352, USA*

⁵*Instituto de Astrofísica de Canarias, E-38205 La Laguna, Tenerife, Spain*

⁶*Universidad de La Laguna, Dept. Astrofísica, E-38206 La Laguna, Tenerife, Spain*

⁷*Department of Physics and Wisconsin IceCube Particle Astrophysics Center, University of Wisconsin-Madison, Madison, WI 53706, USA*

Accepted XXX. Received YYY; in original form ZZZ

ABSTRACT

The extragalactic high-energy γ -ray sky is dominated by blazars, which are active galactic nuclei with their jets pointing towards us. Distance measurements are of fundamental importance yet for some of these sources are challenging because any spectral signature from the host galaxy may be outshone by the non-thermal emission from the jet. In this paper, we present a method to constrain redshifts for these sources that relies only on data from the Large Area Telescope on board the *Fermi Gamma-ray Space Telescope*. This method takes advantage of the signatures that the pair-production interaction between photons with energies larger than approximately 10 GeV and the extragalactic background light leaves on γ -ray spectra. We find upper limits for the distances of 303 γ -ray blazars, classified as 157 BL Lacertae objects, 145 of uncertain class, and 1 flat-spectrum-radio quasar, whose redshifts are otherwise unknown. These derivations can be useful for planning observations with imaging atmospheric Cherenkov telescopes and also for testing theories of supermassive black hole evolution. Our results are applied to estimate the detectability of these blazars with the future Cherenkov Telescope Array, finding that at least 21 of them could be studied in a reasonable exposure of 20 h.

Key words: galaxies: active – BL Lacertae objects: general – gamma-rays: galaxies – galaxies: distances and redshifts

1 INTRODUCTION

Active galactic nuclei that have jets pointing in the direction of our line of sight are known as blazars. These sources dominate the extragalactic sky at the energies detected by the Large Area Telescope (LAT) on board the *Fermi Gamma-ray Space Telescope*, typically around 1 GeV (Ackermann et al. 2016; Abdollahi et al. 2020).

About 50% of the blazars that are catalogued by the LAT collaboration do not have a redshift (Ajello et al. 2020; Abdollahi et al. 2022). This may be caused by a lack of observations, or the absence of spectral features in their optical spectra. However, distance information is critical for different science cases such as (1) building the luminosity function of blazars and understanding their evolution (e.g., Ajello et al. 2012; Ajello et al. 2014, 2015; Sheng et al. 2022), (2) studying emission mechanisms and physical properties (e.g., van den Berg et al. 2019; Paliya et al. 2018, 2021; Nievas Rosillo et al. 2022), or (3) selecting potential targets for imaging atmospheric telescopes including the Cherenkov Telescope Array (e.g., Hassan et al. 2017; Paiano et al. 2021). Measuring these redshifts remains a

challenge despite the important efforts being made to alleviate this problem (e.g., Paggi et al. 2014; Massaro et al. 2015; Landoni et al. 2015; Álvarez Crespo et al. 2016; Klindt et al. 2017; Paiano et al. 2017c; Marchesini et al. 2019; Desai et al. 2019; Paliya et al. 2020; Rajagopal et al. 2021; Goldoni et al. 2021; Olmo-García et al. 2022; Kasai et al. 2023).

Given the observational difficulties, alternative methodologies that are not based on spectral measurements have appeared such as estimating photometric redshifts (e.g., Kaur et al. 2017, 2018; Rajagopal et al. 2020, 2021), finding associated galaxy groups (e.g., Torres-Zafra et al. 2018), or using machine learning techniques (e.g., Coronado-Blázquez 2023). Another possibility is using a combination of data from ground-based imaging atmospheric Cherenkov telescopes and the LAT (Prandini et al. 2010; Yang & Wang 2010; Acciari et al. 2023). This latter technique is based on the phenomenon that γ -ray photons coming from cosmological distances interact by pair-production with the extragalactic background light (EBL, e.g., Hauser & Dwek 2001; Driver et al. 2008; Dwek & Krennrich 2013; Driver 2021; Saldana-Lopez et al. 2021), leaving a signature in the γ -ray spectra that is dependent on the γ -ray photon energy and redshift (e.g., Ackermann et al. 2012; Abramowski et al. 2013; Domínguez & Ajello 2015; Biteau & Williams 2015; Abdalla et al. 2017; Abdollahi et al. 2018; Acciari et al. 2019; Abey-

* E-mail: alberto.d@ucm.es

† E-mail: malainez@ucm.es

‡ E-mail: vaidehi.s.paliya@gmail.com

sekara et al. 2019; Desai et al. 2019; Franceschini 2021; Biteau & Meyer 2022). However, blazars tend to be rather variable sources, which makes combining often non-simultaneous data from different telescopes difficult and subject to systematic biases.

In this paper, we propose a methodology based solely on LAT data and EBL attenuation to set upper limits on the redshifts of blazars. This work is organized as follows. Section 2 includes a brief review on the theoretical aspects about γ -ray attenuation. In Section 3, we describe the γ -ray sample, data reduction, and methodology. This is followed by Section 4, where our results are shown and discussed. Finally, we summarize and conclude in Section 5.

2 THEORETICAL BACKGROUND ON γ -RAY ATTENUATION

We refer the reader to other detailed papers on the theoretical background on γ -ray attenuation such as Dwek & Krennrich (2013) and Finke et al. (2022), and briefly summarize the main aspects here.

There is a pair production interaction between γ rays and EBL photons that produces an optical depth $\tau(E, z)$ that is analytically given by

$$\tau(E, z) = \int_0^z \left(\frac{dl}{dz'} \right) dz' \int_0^2 d\mu \frac{\mu}{2} \int_{\varepsilon_{th}}^{\infty} d\varepsilon' \sigma_{\gamma\gamma}(\beta') n(\varepsilon', z'), \quad (1)$$

where E and z are respectively the observed energy and redshift of the γ -ray source, $\sigma_{\gamma\gamma}$ is the photon-photon pair production cross section and $n(\varepsilon', z')$ is the proper number density of EBL photons with rest-frame energy ε' at redshift z' given by

$$\varepsilon' n(\varepsilon', z') = \frac{4\pi}{c\varepsilon'} \lambda I_{\lambda}(hc/\varepsilon', z'). \quad (2)$$

where λI_{λ} is the EBL spectral intensity. The cross section $\sigma_{\gamma\gamma}$ depends on the relative rest-frame energies of the γ -ray photon (E'), the rest mass energy of the electron $m_e c^2$, and the EBL photon energy (ε') as

$$\beta' = \frac{\varepsilon_{th}}{\varepsilon'}, \quad (3)$$

where ε_{th} is the energy threshold for photon-photon pair production, which is given by

$$\varepsilon_{th} \equiv \frac{2m_e^2 c^4}{E' \mu} \quad (4)$$

and variable $\mu = (1 - \cos \theta)$ connects the energy threshold to the angle of interaction θ .

While γ -ray absorption due to the EBL does not have a fixed onset and strongly depends on redshift, a pragmatic choice of 10 GeV as a threshold can be made when considering blazars in the $z = 2 - 3$ range. The observational effect is that this EBL attenuation leaves a characteristic signature on the γ -ray spectra of blazars (e.g., Ackermann et al. 2012; Abdollahi et al. 2018).

3 SAMPLE SELECTION, DATA REDUCTION, AND METHODOLOGY

3.1 Source selection

For our analysis, we select all blazars in the 4FGL-DR2 catalogue (Ballet et al. 2020). There are several definitions in use to distinguish BL Lacertae objects (BL Lacs) and flat spectrum radio quasars (FSRQs), but the most common one is as follows. Blazars are classified

as BL Lacs if the equivalent width of their emission lines is $< 5 \text{ \AA}$ and FSRQs otherwise (Marcha et al. 1996; Healey et al. 2008). BL Lacs are expected to be the best targets for EBL studies since these are the sources exhibiting a hard γ -ray spectrum and unlikely to have an external photon field, e.g., broad line region (BLR), that may lead to additional γ -ray attenuation (e.g., Domínguez & Ajello 2015). Although, Abdollahi et al. (2018) show that internal absorption is unlikely to be significant for FSRQs, a result confirmed by Costamante et al. (2018). In the LAT catalogues there are also sources classified as blazar candidates of uncertain type (BCUs), which are objects that have a broad-band spectral energy distribution typical of blazars but do not have a spectral classification (Ajello et al. 2020).

Emissions from blazars can present variability producing changes of flux and modifications in the spectrum (e.g., Peñil et al. 2020, 2022; Otero-Santos et al. 2022). These effects may lead to inconclusive results for information extracted from individual spectra using γ -ray attenuation (see for instance the section on Variability in the Supplementary Material by Abdollahi et al. 2018), therefore in our approach we will distinguish between variable and non-variable blazars. This distinction is made using the Variability_Index column in 4FGL-DR2 and using the condition lower or higher than 18.48 as explained by Abdollahi et al. (2020). A higher value corresponds to a 99% probability of the source being variable.

Before making any calculations, we expected that our results would be significant only for BL Lacs and BCUs that are probably BL Lacs, since these sources typically have the strongest EBL signature. However we also ran the method on FSRQs as a sanity check. The initial number of sources in our sample was (non-variable/variable blazars) 621/510 BL Lacs, 866/446 BCUs, and 129/565 FSRQs.

3.2 Data reduction and methodology

For each source in our sample, we develop a LAT analysis as follows:

(i) We perform an analysis in the 1 GeV to 2 TeV range without an EBL model, in order to determine the parameters that define the spectral function such as index and flux, also known as spectral parameters, of the sources around the source of interest. The spectral functions are either PowerLaw or LogParabola models depending on the best fit provided by 4FGL (see below for details).

(ii) We perform an analysis in the 1–10 GeV range without an EBL model, using the source spectral parameters (other than the source of interest) frozen to the values from step (i). The upper limit of 10 GeV is adopted considering the fact that the EBL absorption is negligible below this energy (Ackermann et al. 2012; Abdollahi et al. 2018).

(iii) We extrapolate the spectrum from (ii) to 2 TeV, and include absorption with the EBL model, assuming a redshift of $z = 0.01$, and record the log-likelihood value. We repeat this step for all redshifts between $z = 0.01$ and $z = 3.00$ in 100 steps and save the log-likelihood value at each redshift.

(iv) We compare the log-likelihood values from step (iii) with the one from step (i) to create a TS profile. The peak of this profile gives the most likely value for the redshift. We take this redshift to be an upper limit. Because there can be a component in the spectral curvature of the sources that is not produced by EBL attenuation but which is intrinsic to their emission.

A detailed description of this analysis is as follows. We perform a standard likelihood analysis on the *Fermi*-LAT data covering a given time period (first 14 years of telescope time), energy range (from 1 GeV to 2 TeV), and a selected region of interest (ROI) using *fermiPy* (Wood et al. 2017). The 4FGL catalogue of *Fermi*-LAT

detected sources Data Release 2 (Abdollahi et al. 2020; Ballet et al. 2020) is used to model the γ -ray sky including the latest interstellar emission model (*gll_iem_v07.fits*) and the standard template for the isotropic emission (*iso_P8R3_SOURCE_V2_v1.txt*). We have in the likelihood fitting all 4FGL-DR2 sources lying within the size of the circular region of interest (ROI) plus a radius R . The ROI size as well as R depend on the minimum energy (E_{\min}) of the analysis. Since the point spread function of the *Fermi*-LAT improves considerably at 1 GeV compared to that at the usually adopted $E_{\min} = 100$ MeV, we considered an ROI with radius of 7° and $R = 3^\circ$. Spectral parameters associated with the sources lying outside the ROI are kept fixed, whereas those within the ROI are allowed to vary during the likelihood fitting. For each source, we use the same spectral model as adopted in the 4FGL-DR2 catalog. After the first round of the optimization, the ROI is scanned to search for unmodeled γ -ray sources by generating test statistic (TS) maps. The maximum likelihood TS is defined as $TS = 2\log(L_1/L_0)$, where L_0 and L_1 denote the likelihood values of the null hypothesis (i.e., no source at the position of interest) and that of the alternative hypothesis (i.e., the existence of a point source), respectively (Mattox et al. 1996). When an excess emission ($TS > 25$) is found, it is added to the sky model following a power-law spectral model and, iteratively, a second set of TS maps is generated. A final likelihood fit is performed to optimize all the free parameters in the ROI once all excesses above the background are identified and inserted to the model to optimize the sky model as best as possible. This procedure is necessary since our data are taken in longer exposure than those from which the 4FGL-DR2 sky maps were constructed.

Next, we freeze the spectral parameters of all sources to their best-fitted values except for the source of interest. Then, we apply the EBL attenuation to the spectral model of the source of interest. For this purpose, we update the spectral model of the blazar either to *EBLAtten::PowerLaw2* or *EBLAtten::LogParabola* depending on whether the 4FGL-DR2 spectrum of the blazar reveals a significant curvature or not, which is given by the *Spectrum_Type* column (see Abdollahi et al. 2020; Ballet et al. 2020, for details). In particular, the EBL attenuation is inserted in the spectral *PowerLaw2* or *LogParabola* models¹ as $\exp[-\tau(E, z)]$, where τ is the EBL optical depth as a function of the energy of the γ -ray photon and the redshift, z . In the first step, we use $\tau = 0$, i.e., no EBL, and perform the likelihood fitting in the energy range 1–10 GeV. This exercise enables us to determine the intrinsic shape of the γ -ray spectrum, including any possible curvature. Then, we extrapolate the fitted spectrum to 2 TeV and allow the EBL optical depth to vary in the likelihood fit by changing the redshift value from $z = 0.01$ to $z = 3$ in 100 linear steps. In every step, the log-likelihood value is calculated thus permitting us to generate a likelihood profile as a function of redshift for each blazar in the sample.

Later, we create a different TS profile by comparing this likelihood as a function of redshift with the likelihood from the null hypothesis of no EBL. Therefore, this TS is related to the EBL strength. The peak of the TS profile (TS_{peak}) corresponds to the maximum-likelihood value of the redshift of the target blazar, which, due to previous considerations on the possible intrinsic curvature of the spectra, should be interpreted as an upper limit. We remove from our results (1) all sources with $TS_{peak} < 1$ since these correspond to noisy profiles and 2) those sources whose likelihood profiles do not show a peak in the 0.01–3 redshift range. We determine confidence limits from the

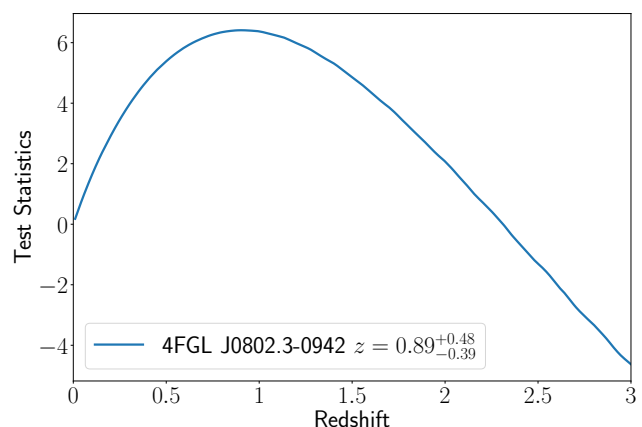


Figure 1. An example of one of the TS profiles. This is the case of 4FGL J0802.3-0942 with $TS_{peak} = 38.3$. Note that negative TS, but not negative TS_{peak} , are possible at the highest redshifts and they mean that the alternate hypothesis of having a point source with γ -ray spectrum attenuated by EBL at a given redshift is disfavoured w.r.t. to that of having no EBL. This may be an indication that the EBL model overestimates the attenuation at these redshifts.

TS profile. Figure 1 shows an example of one likelihood profile, in particular, for 4FGL J0802.3-0942.

For estimating the impact on the redshifts due to the uncertainties of the intrinsic spectrum, we implement a Markov Chain Monte Carlo simulation for a subset of test blazars. For each blazar, we generate 100 random values from a Gaussian distribution centered on the best-fit intrinsic slope with a standard deviation equal to its uncertainty. We then rerun the LAT spectral analysis with these values fixed as the intrinsic spectrum. The resultant redshift distributions are consistent with our original results within the statistical uncertainties. For example, for J0540.5+5823, the redshift of TS_{peak} obtained is $z=1.0\pm 0.3$, while from our simulation, we find a redshift distribution whose mean is 1.1 and standard deviation 0.4. Similar consistency is observed for the other blazars we tested, indicating that the impact of the statistical uncertainties on the redshift limits is minimal. These results hold at a 68% confidence level, reinforcing the robustness of our original findings.

4 RESULTS AND DISCUSSION

4.1 Redshift upper limits

There are 344/331 non-variable/variable sources that satisfy the criteria that are given at the end of Section 3.2. From this sample, there are 5/40 non-variable/variable FSRQs, all of them, with redshifts in the 4LAC catalogue (Ajello et al. 2020), except 4FGL J1532.7-1319. However, we note that this source is classified as BCU in the SIMBAD database².

Then, we have 338/293 non-variable/variable sources (BL Lacs and BCUs), from which 166/162 have a redshift in the 4LAC catalogue and 172/130 do not have a redshift. As a sanity check we plot in Figure 2, the redshift obtained from our EBL-attenuation methodology versus the one in 4LAC for the 166 sources with redshift and $TS_{peak} \geq 1$, and also for the 91 sources with redshift and $TS_{peak} \geq 4$. Figure 3 shows similar information for the variable

¹ https://fermi.gsfc.nasa.gov/ssc/data/analysis/scitools/source_models.html

² <https://cds.u-strasbg.fr/>

blazars, 162 with $TS_{peak} \geq 1$ and 111 with $TS_{peak} \geq 4$. We can see empirically for both sub-samples that the redshift obtained from our methodology can be considered an upper limit for the redshift of the sources in both cases. This is expected since there can be a component in the spectral curvature of the sources that is not produced by EBL attenuation but which is intrinsic to their emission. We tested whether our results change when they are extracted from different periods for the variable sources, concluding that the redshift upper limit generally varies significantly. However in the vast majority of cases, from the comparison with known redshifts, the result is still an upper limit. Furthermore, the empirical test shown in Figure 3 also supports the validity of our upper limits.

For the non-variable blazars, and the case with $TS_{peak} \geq 1$ (and also $TS_{peak} \geq 4$), there is only one source that is away from the one to one line by more than 1σ , which are also within the statistical expectations. This source is Ton 116 ($z_{4LAC} = 1.065$ vs. $z_{EBL} < 0.632$ at 84% C.L., $TS_{peak} = 5.69$). The redshift of Ton 116 given by SIMBAD comes from Abazajian et al. (2009). We could not see any feature leading to that redshift and we think that it could have been automatically assigned by the line search pipeline, probably with low significance. Yet there is a lower limit by Paiano et al. (2017c) at $z > 0.48$ that is compatible with our upper limit of $z_{EBL} < 0.632$ (84% C.L.).

In the case of the variable blazars there are eight blazars that are away from the one to one line more than 1σ (although all within 2σ), also in agreement with statistical expectations. These sources are:

- 3C 66A ($z_{4LAC} = 0.444$ vs. $z_{EBL} < 0.150$ at 84% C.L., $TS_{peak} = 1.66$). The $z_{4LAC} = 0.444$ value comes from very weak lines reported in Miller et al. (1978); Kinney et al. (1991), and Lanzetta et al. (1993). Based on the marginal detection of the host galaxy by Wurtz et al. (1996), Finke et al. (2008) estimated the redshift to be $z = 0.321$. However, Stadnik & Romani (2014) were not able to detect the host galaxy and, based on this non-detection, gave a lower limit of $z > 0.42$. In SIMBAD, the reported value for the redshift of this source is $z_{SIMBAD} = 0.340$, using the HI column density (Neeleman et al. 2016). Based on a comparison of the LAT and MAGIC spectrum, and assuming EBL attenuation, Aleksić et al. (2011) estimated the redshift $z < 0.68$. Recently, Paiano et al. (2017a) observed the optical spectra of 3C 66A in a spectroscopic campaign carried out at the 10 m Gran Telescopio Canarias, leading to inconclusive results. To this date, the redshift of this source remains a subject of debate.

- IES 0502+675 ($z_{4LAC} = 0.416$ vs. $z_{EBL} < 0.331$ at 84% C.L., $TS_{peak} = 54.39$). As for the previous case, the redshift reported in SIMBAD is different from the value that appears in the 4LAC. In 4LAC, the redshift value $z_{4LAC} = 0.416$ is taken from Landt et al. (2002), while in SIMBAD the value $z_{SIMBAD} = 0.314$ is selected from Sbarufatti et al. (2005), that is compatible with the upper limit here derived. However, these studies rely on imaging methods, since there is no optical spectrum available for this source.

- TXS 0628–240 ($z_{4LAC} = 1.238$ vs. $z_{EBL} < 1.124$ at 84% C.L., $TS_{peak} = 45.70$). The redshift comes from Landt (2012), which actually gives a lower limit based on a clear Mg II absorption line. This $z > 1.238$ limit is similar to our upper limit of $z_{EBL} < 1.124$ (84% C.L.), likely indicating that the Mg II line actually comes from the BL Lac host galaxy instead of an intercepting gas cloud.

- NVSS J090226+205045 ($z_{4LAC} = 2.055$ vs. $z_{EBL} < 1.274$ at 84% C.L., $TS_{peak} = 5.44$). The 4LAC redshift is taken from the automatic line finding pipeline given by the SDSS DR6 (Richards et al. 2009), which can be biased for faint lines as are typical in BL Lacs. However, there are no emission/absorption lines in the spectra

that allow its confirmation. A more recent upper limit for the redshift of this object is available in the literature: $z < 1.21$ given by Rau et al. (2012) using UV-to-NIR photometry.

- PKS 0903-57 ($z_{4LAC} = 0.695$ vs. $z_{EBL} < 0.451$ at 84% C.L., $TS_{peak} = 7.82$). This value is selected from optical spectroscopic observations performed by Thompson et al. (1990). However, these authors select the position of the source by its radio emission, and they mention that the optical counterpart corresponding to the radio emission is a star, so the optical spectra they took corresponds to a source 4 arcsec west of the position of the radio emission, a Seyfert I. Therefore, it would be necessary to re-observe the optical spectra for this object, to see whether the optical counterpart observed to determine the value $z = 0.695$ is correct or is a different source.

- 87GB 105148.6+222705 ($z_{4LAC} = 2.055$ vs. $z_{EBL} < 1.274$ at 84% C.L., $TS_{peak} = 6.71$). As in the previous case, the 4LAC redshift value is taken from the SDSS DR6 (Richards et al. 2009), while this value is assigned automatically with poor significance. Rau et al. (2012) gave an upper limit of $z < 1.36$, and there is a more recent value given automatically by the SDSS DR13³ for this object: $z = 0.63$, both compatible with the upper limit presented here.

- PKS 1424+240 ($z_{4LAC} = 0.604$ vs. $z_{EBL} < 0.431$ at 84% C.L., $TS_{peak} = 25.17$). This redshift is obtained by Paiano et al. (2017b) from some weak emission lines. Rovero et al. (2016) identifies this BL Lac as a member of a galaxy cluster at $z = 0.601$.

- MG3 J225517+2409 ($z_{4LAC} = 1.370$ vs. $z_{EBL} < 0.752$ at 84% C.L., $TS_{peak} = 2.77$). The 4LAC redshift value is from Albareti et al. (2017), but we did not identify any feature leading to that redshift and we think that it could have been automatically assigned, probably with small significance.

Since the upper limit interpretation is robust for non-variable as well as for variable sources, we do not distinguish between them in the following discussions. Table 1 lists the 303 blazars that do not have a redshift in 4LAC and whose likelihood profile peaks at $z < 3$. We stress that the 125 sources with $1 \leq TS_{peak} < 4$ correspond to a significance lower than 2σ , which according to Figure 2 seem to be compatible with upper limits as well. At any rate, although we give these low significance results ($TS_{peak} < 4$) in Table 1, we suggest the user be prudent about using them.

Figure 4 shows the 303 sources listed in Table 1 in comparison with our initial source selection. It is clear that these blazars lie in the lower region of the initial sample cloud, where, as expected, they tend to have a lower photon index, i.e., hard spectrum.

In Figure 5, we show the 303 blazars using the redshift upper limit at 84% C.L. along the cosmic γ -ray horizon (CGRH), this is the energy as a function of redshift for which $\tau = 1$. This implies CGRH divides the universe in two different regions for which the surviving flux is larger or smaller than $\exp(-1) \sim 37\%$. The upper limits that lie around the most opaque regions, such as at $z \sim 2.5$ and energies of approximately 200 GeV are poorly constrained.

In order to estimate the uncertainties introduced by the EBL, we also run our pipeline using the lower uncertainties of the optical depths given by Domínguez et al. (2023) based on the model by Saldana-Lopez et al. (2021). These lower uncertainties will translate into larger values of the redshift where the TS profile peaks, which goes from smaller shifts in TS_{peak} for the lower redshifts and larger for the higher redshifts. This effect is a consequence of having better constrained the EBL at the lower than at the higher redshifts. The increase in the redshifts where TS_{peak} is, in redshift bins of 0.5 from $z = 0$ to $z = 3$, is on average approximately 13%, 16%, 21%, 28%,

³ https://www.sdss.org/dr13/data_access/bulk/

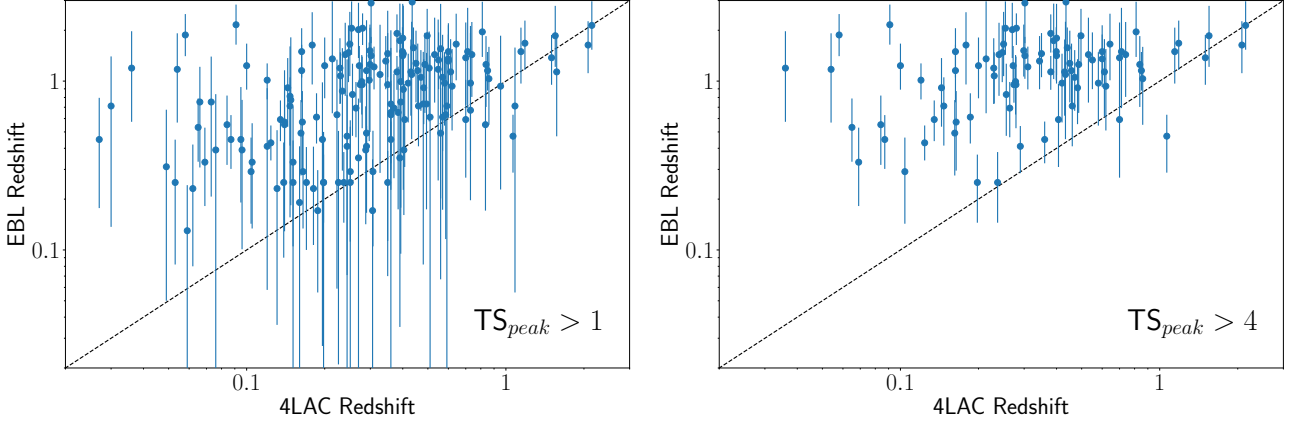


Figure 2. Redshift from our EBL methodology for non-variable blazars (*Left panel*) for the 166 sources with redshift in 4LAC and $TS_{peak} \geq 1$ and (*Right panel*) the 91 sources with redshift in 4LAC and $TS_{peak} \geq 4$. The uncertainties at lower redshifts, $z < 0.5$, can be larger than the ones at higher redshifts, $z \sim 1$, because at the lower redshifts, the EBL affects energies larger than 200–300 GeV where the LAT’s effective area is smaller.

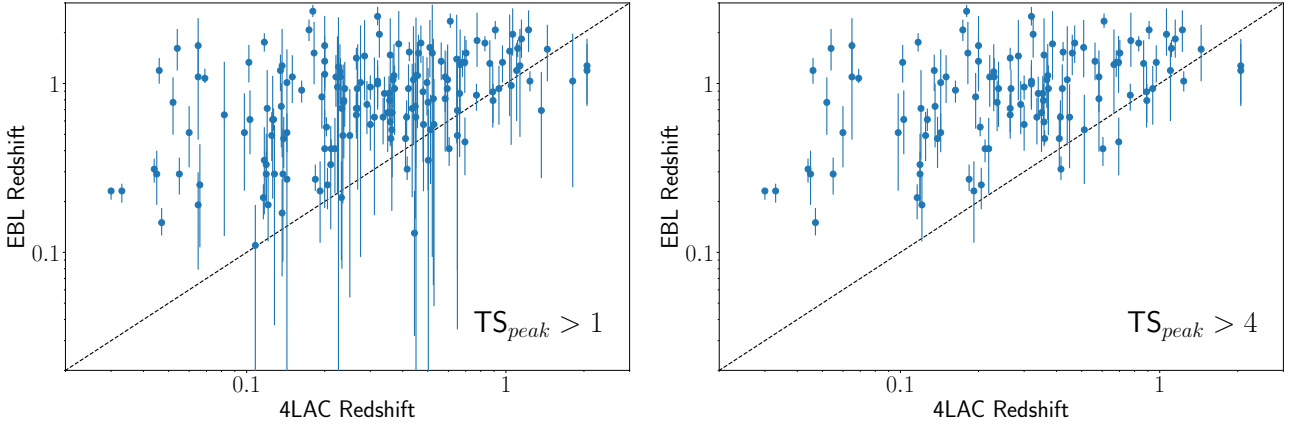


Figure 3. Redshift from our EBL methodology for variable blazars (*Left panel*) for the 162 sources with redshift in 4LAC and $TS_{peak} \geq 1$ and (*Right panel*) the 111 sources with redshift in 4LAC and $TS_{peak} \geq 4$. See comment in the previous figure about the uncertainties.

26% and 30%, respectively. We stress that the redshifts upper limits obtained for other models such as [Finke et al. \(2010\)](#), [Domínguez et al. \(2011\)](#), [Franceschini & Rodighiero \(2017\)](#) and [Finke et al. \(2022\)](#) are within these uncertainties. Any larger intensity EBL will not affect the redshifts upper limits because a more opaque universe leads to lower redshifts for the TS_{peak} . Furthermore, we tested that TS_{peak} tend to be larger for [Domínguez et al. \(2023\)](#) than for [Domínguez et al. \(2011\)](#) indicating that the former model produces better fits, as expected since it is based on deeper and extended multiwavelength data.

4.2 Application case: detectability predictions for the Cherenkov Telescope Array

The redshift upper limits are used to compute the expected detection significance of the 303 sources listed in Table 1 with the Cherenkov Telescope Array (CTA, [Acharya et al. 2019](#)) using a total exposure of 20 hours, a reasonable exploratory time for IACTs. For the estimate of the source detectability, we use the CTA instrument response functions⁴ (IRFs) for the Alpha configuration with average azimuth

angle, which are available for three different zenith angles (i.e., 20 deg, 40 deg and 60 deg), both for the northern and southern arrays. The CTA-North and CTA-South IRFs are used for the sources with positive and negative declination, respectively. We assume observations around culmination time to select the most adequate IRF configuration concerning the zenith angle. We have generated point-like differential sensitivity curves for a total exposure time of 20 hours by scaling the IRFs corresponding to an exposure of 5 hours utilizing `gammapy` ([Deil et al. 2017](#); [Acero et al. 2022](#)). As products from this calculation we obtained the differential flux, number of excess events, and number of background events that would generate a 5σ signal in each energy bin. This is then used to obtain the expected number of excess events for each considered source, which is computed by scaling linearly the number of excess events necessary to get a detection significance of 5σ with the ratio of the differential flux. This is the differential flux of the sensitivity curve for each energy bin. The obtained number of excess and background events are used to estimate the statistical detection significance of the blazars using the function `WStatCountsStatistic` of `gammapy`, which applies the formula derived by [Li & Ma \(1983\)](#). The energy threshold in each case is selected as the energy of the lower bin of the corresponding differential sensitivity curve, i.e. the energy threshold is

⁴ <https://zenodo.org/record/5499840>

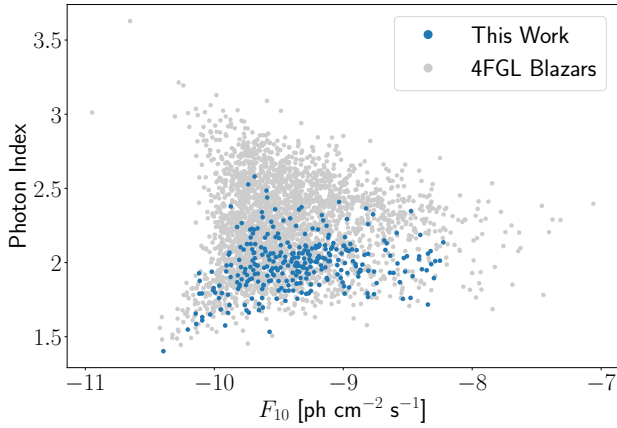


Figure 4. Photon index versus integrated flux at energies above 10 GeV from the initial sample (grey symbols) and the 303 blazars for which we find a redshift upper limit (blue symbols).

considered larger for sources that can only be observed with a zenith angle > 50 deg and also for sources observed with CTA-South.

For the source’s spectral shape, we consider the result from the LAT data analysis at the redshift upper limit, which we stress is a PowerLaw or LogParabola including the EBL exponential attenuation. This spectral shape is extrapolated to TeV energies considering the EBL absorption following the optical depths by Domínguez et al. (2023) based on the recent model by Saldana-Lopez et al. (2021), consistent with our LAT data reduction. The significance is estimated using as the redshift of the source, the upper limit values at 84% C.L. from Table 1; this is the redshift of the TS_{peak} plus upper uncertainties. For these calculations we use the best zenith angle for the observation either from CTA-North or CTA-South. This results in a total of 21 sources with an expected significance of $> 5\sigma$. We stress that this refers to detections in the average/quiescent state of the source derived from the average flux over 14 years of *Fermi*-LAT telescope time. Note that considering only the redshift of the TS_{peak} , which can be a reasonable approach according to Figure 2, there are 41 sources with a significance of $> 5\sigma$. These additional 20 sources are J0143.7-5846, J0322.0+2335, J0333.9+6537, J0334.2-3725, J0338.5+1302, J0338.9-2848, J0540.5+5823, J0600.3+1244, J0709.2-1527, J0812.0+0237, J0826.4-6404, J1240.4-7148, J1253.2+5301, J1454.4+5124, J1518.0-2731, J1553.5-3118, J1610.7-6648, J1704.5-0527, J2104.3-0212 and J2247.8+4413. We stress that, since we use redshift upper limits in our computation, these CTA detection significances can be considered lower limits. If the sources were closer, the EBL attenuation would be less, so the very-high-energy emission ($E > 50$ GeV) from the sources would be brighter, and they would be easier for CTA to detect.

5 SUMMARY AND CONCLUSIONS

We have calculated redshift upper limits for 303 γ -ray blazars using LAT data and EBL attenuation. The majority of these blazars are classified as BL Lacs. The redshifts derived with our methodology can be useful for studying the evolution of blazars or planning observations with other telescopes, for instance, with imaging atmospheric Cherenkov telescopes such as MAGIC, VERITAS, H.E.S.S and CTA. We find that 21 blazars, for which we have found a redshift

upper limit, can be detected in their average/quiescent state with CTA in 20h.

ACKNOWLEDGEMENTS

The *Fermi*-LAT Collaboration acknowledges generous ongoing support from a number of agencies and institutes that have supported both the development and the operation of the LAT as well as scientific data analysis. These include the National Aeronautics and Space Administration and the Department of Energy in the United States, the Commissariat à l’Energie Atomique and the Centre National de la Recherche Scientifique / Institut National de Physique Nucléaire et de Physique des Particules in France, the Agenzia Spaziale Italiana and the Istituto Nazionale di Fisica Nucleare in Italy, the Ministry of Education, Culture, Sports, Science and Technology (MEXT), High Energy Accelerator Research Organization (KEK) and Japan Aerospace Exploration Agency (JAXA) in Japan, and the K. A. Wallenberg Foundation, the Swedish Research Council and the Swedish National Space Board in Sweden.

Additional support for science analysis during the operations phase is gratefully acknowledged from the Istituto Nazionale di Astrofisica in Italy and the Centre National d’Études Spatiales in France. This work was performed in part under DOE Contract DE-AC02-76SF00515.

This research has made use of the CTA instrument response functions provided by the CTA Consortium and Observatory, see <https://www.ctao-observatory.org/science/cta-performance/> (version prod5 v0.1; Cherenkov Telescope Array Observatory and Cherenkov Telescope Array Consortium 2021) for more details.

We thank Daniel Nieto for providing computational resources, David Paneque for helpful comments, and Jonathan Biteau for a constructive review. A.D. is thankful for the support of the Ramón y Cajal program from the Spanish MINECO, Proyecto PID2021-126536OA-I00 funded by MCIN / AEI / 10.13039/501100011033, and Proyecto PR44/21-29915 funded by the Santander Bank and Universidad Complutense de Madrid. J.F. is partially supported by NASA through contract S-15633Y. M.L. is funded by MCIN through grant PRE2020-093502. J.L.C. is supported by MCIN project PID2019-104114RB-C32. J.F. is partially supported by NASA through contract S-15633Y.

DATA AVAILABILITY

The results of this study are publicly available at <https://www.ucm.es/blazars/zebl> and by request to the authors.

REFERENCES

- Abazajian K. N., et al., 2009, *ApJS*, 182, 543
- Abdalla H., et al., 2017, *A&A*, 606, A59
- Abdollahi S., et al., 2018, *Science*, 362, 1031
- Abdollahi S., et al., 2020, *ApJS*, 247, 33
- Abdollahi S., et al., 2022, *ApJS*, 260, 53
- Abeysekera A. U., et al., 2019, *ApJ*, 885, 150
- Abramowski A., et al., 2013, *A&A*, 550, A4
- Acciari V. A., et al., 2019, *MNRAS*, 486, 4233
- Acciari V. A., et al., 2023, *A&A*, 670, A49
- Acero F., et al., 2022, Gammapy: Python toolbox for gamma-ray astronomy, doi:10.5281/zenodo.7311399, <https://doi.org/10.5281/zenodo.7311399>

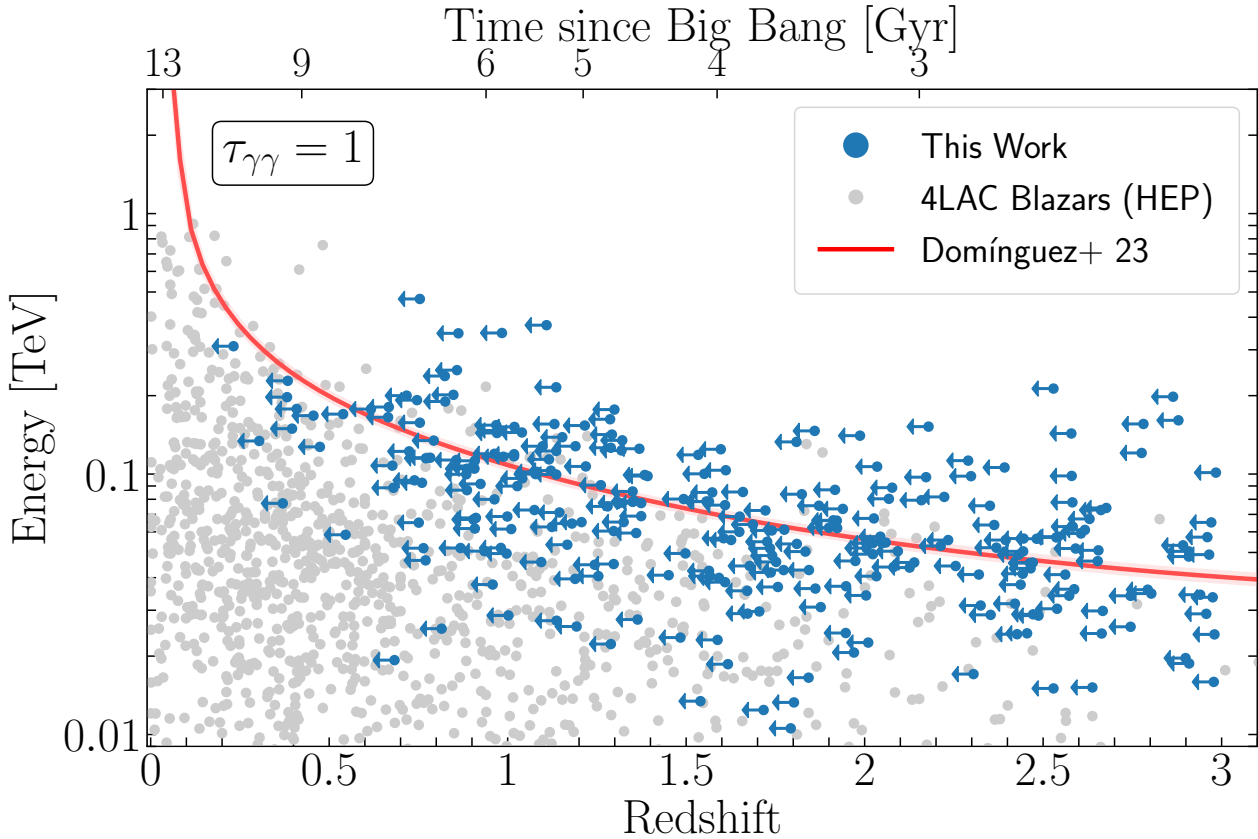


Figure 5. Highest energy photons of 4LAC blazars (grey circles) as a function of redshift, the cosmic γ -ray horizon from Domínguez et al. (2023, red band) based on the EBL model by Saldana-Lopez et al. (2021), and the upper limits at 84% C.L. from this work (blue circles). We find upper limits for the redshifts of 303 blazars.

Acharya B. S., et al., 2019, Science with the Cherenkov Telescope Array, doi:10.1142/10986.

Ackermann M., et al., 2012, Science, 338, 1190

Ackermann M., et al., 2016, ApJS, 222, 5

Ajello M., et al., 2012, ApJ, 751, 108

Ajello M., et al., 2014, ApJ, 780, 73

Ajello M., et al., 2015, ApJ, 800, L27

Ajello M., et al., 2020, ApJ, 892, 105

Albareti F. D., et al., 2017, ApJS, 233, 25

Aleksić J., et al., 2011, A&A, 530, A4+

Álvarez Crespo N., et al., 2016, AJ, 151, 95

Ballet J., Burnett T. H., Digel S. W., Lott B., 2020, arXiv e-prints, p. arXiv:2005.11208

Biteau J., Meyer M., 2022, Galaxies, 10, 39

Biteau J., Williams D. A., 2015, ApJ, 812, 60

Cherenkov Telescope Array Observatory and Cherenkov Telescope Array Consortium 2021, CTAO Instrument Response Functions - prod5 version v0.1, doi:10.5281/zenodo.5499840, https://doi.org/10.5281/zenodo.5499840

Coronado-Blázquez J., 2023, MNRAS, 521, 4156

Costamante L., Cutini S., Tosti G., Antolini E., Tramacere A., 2018, MNRAS, 477, 4749

Deil C., et al., 2017, in 35th International Cosmic Ray Conference (ICRC2017), p. 766 (arXiv:1709.01751), doi:10.22323/1.301.0766

Desai A., Helgason K., Ajello M., Paliya V., Domínguez A., Finke J., Hartmann D., 2019, ApJ, 874, L7

Domínguez A., Ajello M., 2015, ApJ, 813, L34

Domínguez A., et al., 2011, MNRAS, 410, 2556

Domínguez A., et al., 2023, arXiv e-prints, p. arXiv:2306.09878

Driver S. P., 2021, arXiv e-prints, p. arXiv:2102.12089

Driver S. P., Popescu C. C., Tuffs R. J., Graham A. W., Liske J., Baldry I., 2008, ApJ, 678, L101

Dwek E., Krennrich F., 2013, Astroparticle Physics, 43, 112

Finke J. D., Shields J. C., Böttcher M., Basu S., 2008, A&A, 477, 513

Finke J. D., Razzaque S., Dermer C. D., 2010, ApJ, 712, 238

Finke J. D., Ajello M., Domínguez A., Desai A., Hartmann D. H., Paliya V. S., Saldana-Lopez A., 2022, arXiv e-prints, p. arXiv:2210.01157

Franceschini A., 2021, Universe, 7, 146

Franceschini A., Rodighiero G., 2017, A&A, 603, A34

Goldoni P., et al., 2021, A&A, 650, A106

Hassan T., Domínguez A., Lefaucheur J., Mazin D., Pita S., Zech A., Consortium C., 2017, in 35th International Cosmic Ray Conference (ICRC2017), p. 632 (arXiv:1708.07704)

Hauser M. G., Dwek E., 2001, ARA&A, 39, 249

Healey S. E., et al., 2008, ApJS, 175, 97

Kasai E., et al., 2023, MNRAS, 518, 2675

Kaur A., et al., 2017, ApJ, 834, 41

Kaur A., Rau A., Ajello M., Domínguez A., Paliya V. S., Greiner J., Hartmann D. H., Schady P., 2018, ApJ, 859, 80

Kinney A. L., Bohlin R. C., Blades J. C., York D. G., 1991, ApJS, 75, 645

Klindt L., van Soelen B., Meintjes P. J., Väisänen P., 2017, MNRAS, 467, 2537

Landoni M., et al., 2015, AJ, 149, 163

Landt H., 2012, MNRAS, 423, L84

Landt H., Padovani P., Giommi P., 2002, MNRAS, 336, 945

Lanzetta K. M., Turnshek D. A., Sandoval J., 1993, ApJS, 84, 109

Li T. P., Ma Y. Q., 1983, ApJ, 272, 317

Marcha M. J. M., Browne I. W. A., Impy C. D., Smith P. S., 1996, MNRAS, 281, 425

Marchesini E. J., et al., 2019, Ap&SS, 364, 5

- Massaro F., Landoni M., D'Abrusco R., Milisavljevic D., Paggi A., Masetti N., Smith H. A., Tosti G., 2015, *A&A*, **575**, A124
- Mattox J. R., et al., 1996, *ApJ*, **461**, 396
- Miller J. S., French H. B., Hawley S. A., 1978, in Wolfe A. M., ed., *BL Lac Objects*. pp 176–187
- Neeleman M., Prochaska J. X., Ribaldo J., Lehner N., Howk J. C., Rafelski M., Kanekar N., 2016, *ApJ*, **818**, 113
- Nievas Rosillo M., Domínguez A., Chiaro G., La Mura G., Brill A., Paliya V. S., 2022, *MNRAS*, **512**, 137
- Olmo-García A., Paliya V. S., Álvarez Crespo N., Kumar B., Domínguez A., Gil de Paz A., Sánchez-Blázquez P., 2022, *MNRAS*, **516**, 5702
- Otero-Santos J., Acosta-Pulido J. A., Becerra González J., Luashvili A., Castro Segura N., González-Martín O., Raiteri C. M., Carnerero M. I., 2022, *MNRAS*, **511**, 5611
- Paggi A., et al., 2014, *AJ*, **147**, 112
- Paiano S., Landoni M., Falomo R., Treves A., Scarpa R., Righi C., 2017a, *ApJ*, **837**, 144
- Paiano S., Landoni M., Falomo R., Treves A., Scarpa R., Righi C., 2017b, *ApJ*, **837**, 144
- Paiano S., Falomo R., Franceschini A., Treves A., Scarpa R., 2017c, *ApJ*, **851**, 135
- Paiano S., Treves A., Franceschini A., Falomo R., 2021, *MNRAS*, **508**, 6128
- Paliya V. S., Zhang H., Böttcher M., Ajello M., Domínguez A., Joshi M., Hartmann D., Stalin C. S., 2018, *ApJ*, **863**, 98
- Paliya V. S., et al., 2020, *ApJ*, **903**, L8
- Paliya V. S., Domínguez A., Ajello M., Olmo-García A., Hartmann D., 2021, *ApJS*, **253**, 46
- Peñil P., et al., 2020, *ApJ*, **896**, 134
- Peñil P., Ajello M., Buson S., Domínguez A., Westernacher-Schneider J. R., Zrake J., 2022, *arXiv e-prints*, p. [arXiv:2211.01894](https://arxiv.org/abs/2211.01894)
- Prandini E., Bonnoli G., Maraschi L., Mariotti M., Tavecchio F., 2010, *MNRAS*, **405**, L76
- Rajagopal M., Kaur A., Ajello M., Rau A., Domínguez A., Cenko B., Greiner J., Hartmann D. H., 2020, *ApJ*, **898**, 18
- Rajagopal M., Marchesi S., Kaur A., Domínguez A., Silver R., Ajello M., 2021, *ApJS*, **254**, 26
- Rau A., et al., 2012, *A&A*, **538**, A26
- Richards G. T., et al., 2009, *ApJS*, **180**, 67
- Rovero A. C., Muriel H., Donzelli C., Pichel A., 2016, *A&A*, **589**, A92
- Saldana-Lopez A., Domínguez A., Pérez-González P. G., Finke J., Ajello M., Primack J. R., Paliya V. S., Desai A., 2021, *MNRAS*, **507**, 5144
- Sbarufatti B., Treves A., Falomo R., 2005, *ApJ*, **635**, 173
- Sheng Y., et al., 2022, *arXiv e-prints*, p. [arXiv:2209.09877](https://arxiv.org/abs/2209.09877)
- Stadnik M., Romani R. W., 2014, *ApJ*, **784**, 151
- Thompson D. J., Djorgovski S., de Carvalho R., 1990, *PASP*, **102**, 1235
- Torres-Zafra J., Cellone S. A., Buzzoni A., Andruchow I., Portilla J. G., 2018, *MNRAS*, **474**, 3162
- Wood M., Caputo R., Charles E., Di Mauro M., Magill J., Perkins J. S., Fermi-LAT Collaboration 2017, in 35th International Cosmic Ray Conference (ICRC2017). p. 824 ([arXiv:1707.09551](https://arxiv.org/abs/1707.09551))
- Wurtz R., Stocke J. T., Yee H. K. C., 1996, *ApJS*, **103**, 109
- Yang J., Wang J., 2010, *PASJ*, **62**, L23
- van den Berg J. P., Böttcher M., Domínguez A., López-Moya M., 2019, *ApJ*, **874**, 47

This paper has been typeset from a $\text{\TeX}/\text{\LaTeX}$ file prepared by the author.

4FGL Source Name (1)	Redshift Upper Limit (2)	TS_{peak} (3)	HEP (GeV) (4)	Type (5)	Association (6)	TeV (7)	CTA (σ) (8)
J0001.2-0747	$1.19^{+0.72}_{-0.61}$	5.1	86	bl	PMN J0001-0746	N	0.7
J0001.6-4156	$0.27^{+0.97}_{-0.25}$	1.2	44	bcu	1RXS J000135.5-415519	N	1.2
J0002.1-6728	$1.66^{+0.71}_{-0.59}$	9.8	52	bcu	SUMSS J000215-672653	N	0.1
J0003.1-5248	$0.51^{+0.41}_{-0.30}$	1.7	91	bcu	RBS 0006	N	1.1
J0009.3+5030	$0.77^{+0.30}_{-0.30}$	4.4	72	bl	NVSS J000922+503028	N	3.0
J0014.7+5801	$1.96^{+0.92}_{-0.58}$	47.4	160	bl	1RXS J001442.2+580201	N	0.6
J0014.8+6118	$2.12^{+0.82}_{-0.66}$	16.27	34	bcu	4C +60.01	N	0.6
J0015.6+5551	$0.27^{+0.18}_{-0.14}$	3.8	167	bl	GB6 J0015+5551	N	3.2
J0017.0-0649	$1.27^{+1.38}_{-1.24}$	1.1	46	bcu	PMN J0017-0650	N	0.1
J0019.3-8152	$1.25^{+0.56}_{-0.57}$	4.8	53	bl	PMN J0019-8152	N	0.0
J0019.6+2022	$1.07^{+1.56}_{-0.94}$	1.3	-	bl	PKS 0017+200	N	0.2
J0021.0+0322	$2.94^{+0.02}_{-1.29}$	12.3	-	bcu	2MASS J00205023+0323578	N	0.3
J0021.5-2552	$1.19^{+0.90}_{-0.72}$	2.7	50	bl	CRATES J002132.55-255049.3	N	0.3
J0022.5+0608	$1.33^{+0.53}_{-0.47}$	7.0	36	bl	PKS 0019+058	N	1.7
J0026.6-4600	$0.61^{+0.53}_{-0.49}$	1.6	71	bl	1RXS J002636.3-460101	N	0.6
J0031.3+0726	$0.99^{+1.06}_{-0.89}$	1.3	54	bl	NVSS J003119+072456	N	0.2
J0035.9+5950	$1.03^{+0.08}_{-0.10}$	739.8	372	bl	1ES 0033+595	Y	38.0
J0040.3+4050	$0.39^{+1.14}_{-0.29}$	2.4	118	bl	B3 0037+405	N	0.8
J0045.7+1217	$0.67^{+0.34}_{-0.29}$	6.4	61	bl	GB6 J0045+1217	N	3.0
J0052.9-6644	$1.76^{+1.05}_{-0.76}$	8.4	-	bcu	PMN J0052-6641	N	0.0
J0115.6+0356	$1.17^{+0.56}_{-0.59}$	4.1	51	bl	PMN J0115+0356	N	1.4
J0116.0-2745	$0.99^{+0.75}_{-0.66}$	2.4	48	bl	1RXS J011555.6-274428	N	0.3
J0116.2-6153	$0.85^{+0.64}_{-0.60}$	2.1	80	bl	SUMSS J011619-615343	N	0.1
J0120.4-2701	$0.79^{+0.20}_{-0.19}$	21.8	116	bl	PKS 0118-272	N	12.3
J0127.2+0324	$1.09^{+0.73}_{-0.59}$	4.1	83	bl	NVSS J012713+032259	N	0.6
J0135.1+0255	$0.87^{+0.69}_{-0.49}$	5.2	78	bcu	1RXS J013506.7+025558	N	0.5
J0136.5+3906	$0.73^{+0.13}_{-0.12}$	35.1	250	bl	B3 0133+388	Y	21.5
J0138.0+2247	$0.47^{+0.44}_{-0.42}$	1.3	67	bl	GB6 J0138+2248	N	1.2
J0140.6+8736	$1.07^{+1.38}_{-0.79}$	2.1	24	bcu	WN B0126.6+8722	N	0.0
J0143.7-5846	$0.77^{+0.20}_{-0.18}$	25.2	154	bl	SUMSS J014347-584550	N	4.3
J0144.6+2705	$2.38^{+0.53}_{-0.39}$	41.0	48	bl	TXS 0141+268	N	2.2
J0148.2+5201	$0.41^{+0.27}_{-0.24}$	2.5	107	bl	GB6 J0148+5202	N	2.0
J0150.6-5448	$0.61^{+0.84}_{-0.56}$	1.2	40	bcu	PMN J0150-5450	N	0.1
J0158.5-3932	$0.59^{+0.60}_{-0.49}$	1.5	39	bl	PMN J0158-3932	N	0.8
J0159.7-2740	$0.77^{+0.59}_{-0.72}$	1.1	27	bl	PMN J0159-2739	N	0.5
J0201.1-4347	$0.91^{+1.06}_{-0.81}$	1.3	20	bcu	GALEXASC J020110.83-434654.8	N	0.1
J0206.8-5744	$0.35^{+0.46}_{-0.34}$	1.0	-	bcu	SUMSS J020640-574948	N	0.7
J0208.3-6838	$1.44^{+1.11}_{-0.72}$	5.5	57	bl	PKS 0206-688	N	0.0
J0209.3+4449	$0.57^{+0.52}_{-0.44}$	2.2	45	bl	1RXS J020917.6+444951	N	1.3
J0215.3+7555	$0.45^{+2.13}_{-0.15}$	14.3	143	bcu	WN B0210.3+7540	N	0.4
J0223.0+6821	$1.31^{+0.73}_{-0.59}$	6.5	57	bl	NVSS J022304+682154	N	0.6
J0224.0-7941	$1.25^{+1.28}_{-1.24}$	1.0	30	bl	PMN J0223-7940	N	0.0
J0226.5-4441	$1.68^{+1.10}_{-0.65}$	11.7	120	bl	RBS 0318	N	0.3
J0233.9+8041	$1.21^{+0.51}_{-0.39}$	20.0	72	bcu	1RXS J023428.6+804341	N	0.2
J0240.8-3401	$0.97^{+1.11}_{-0.79}$	1.6	43	bcu	NVSS J024047-340018	N	0.1
J0241.3+6543	$0.51^{+0.40}_{-0.40}$	1.7	104	bl	TXS 0237+655	N	1.5
J0245.1-0257	$1.01^{+0.74}_{-0.70}$	2.0	45	bl	PMN J0245-0255	N	0.3
J0250.7+5630	$1.68^{+0.77}_{-0.77}$	5.7	50	bcu	RX J0250.7+5629	N	0.6
J0259.3+5453	$1.13^{+0.84}_{-0.76}$	2.6	46	bcu	GB6 J0259+5451	N	0.3
J0303.6+4716	$0.63^{+0.37}_{-0.40}$	2.1	68	bl	4C +47.08	N	2.4
J0307.4+4915	$1.44^{+0.50}_{-0.47}$	9.0	73	bl	GB6 J0307+4915	N	1.2
J0310.6-5017	$0.87^{+0.42}_{-0.41}$	1.7	60	bl	1RXS J031036.0-501615	N	1.1
J0314.3-5103	$1.44^{+0.51}_{-0.60}$	7.5	45	bl	PMN J0314-5104	N	0.4
J0315.4-2643	$0.57^{+0.56}_{-0.44}$	1.8	27	bcu	NVSS J031527-264400	N	0.7
J0316.2-6437	$0.59^{+0.26}_{-0.23}$	9.7	201	bl	SUMSS J031614-643732	N	2.6
J0318.7+2135	$1.38^{+0.70}_{-0.49}$	9.2	88	bl	MG3 J031849+2135	N	1.0
J0322.0+2335	$0.89^{+0.24}_{-0.22}$	20.1	122	bl	MG3 J032201+2336	N	5.0
J0331.9+6307	$0.87^{+0.45}_{-0.46}$	3.6	65	bl	GB6 J0331+6307	N	1.2
J0333.9+6537	$0.79^{+0.25}_{-0.21}$	16.8	96	bl	TXS 0329+654	N	4.9
J0334.2-3725	$1.03^{+0.28}_{-0.27}$	13.6	77	bl	PMN J0334-3725	N	3.6
J0335.1-4459	$0.99^{+0.57}_{-0.51}$	4.3	42	bl	1RXS J033514.5-445929	N	0.6

4FGL Source Name (1)	Redshift Upper Limit (2)	TS _{peak} (3)	HEP (GeV) (4)	Type (5)	Association (6)	TeV (7)	CTA (σ) (8)
J0338.5+1302	0.63 ^{+0.27} _{-0.33}	2.6	66	bll	RX J0338.4+1302	N	4.4
J0338.9-2848	0.43 ^{+0.29} _{-0.23}	3.8	200	bcu	NVSS J033859-284619	N	3.6
J0343.2-6444	1.21 ^{+0.66} _{-0.56}	5.3	75	bll	PMN J0343-6442	N	0.2
J0344.4+3432	0.41 ^{+0.31} _{-0.23}	4.0	122	bcu	1RXS J034424.5+343016	N	1.3
J0348.2+6035	1.74 ^{+0.79} _{-0.74}	15.2	212	bcu	NVSS J034819+603509	N	0.6
J0350.0+0640	1.61 ^{+0.68} _{-0.47}	35.7	112	bcu	RX J0350.0+0640	N	0.0
J0355.3+3909	0.39 ^{+0.42} _{-0.28}	2.2	25	bcu	CRATES J035515+390907	N	1.0
J0410.9+4216	1.76 ^{+1.20} _{-0.88}	3.4	29	bcu	B3 0407+421	N	0.2
J0420.3-6016	0.49 ^{+0.51} _{-0.47}	1.1	49	bcu	1RXS J042012.8-601446	N	0.3
J0423.9+4150	2.16 ^{+0.28} _{-0.27}	199.8	49	bll	4C +41.11	N	6.0
J0425.3+6319	0.51 ^{+0.27} _{-0.27}	3.9	115	bcu	1RXS J042523.0+632016	N	1.9
J0426.7+6826	1.84 ^{+1.06} _{-0.80}	6.4	53	bcu	4C +68.05	N	0.3
J0431.8+7403	1.98 ^{+0.60} _{-0.54}	17.3	77	bll	GB6 J0431+7403	N	0.6
J0434.7+0922	0.53 ^{+0.43} _{-0.39}	2.0	119	bll	TXS 0431+092	N	1.6
J0439.4-3202	1.03 ^{+0.71} _{-0.67}	2.2	60	bcu	1RXS J043931.4-320045	N	0.2
J0442.7+6142	0.47 ^{+0.27} _{-0.29}	3.2	92	bcu	GB6 J0442+6140	N	1.7
J0447.2-2539	0.83 ^{+0.52} _{-0.45}	4.5	78	bcu	2MASS J04472149-2539302	N	0.7
J0451.8+5721	1.25 ^{+0.76} _{-0.82}	2.2	22	bcu	NVSS J045148+572139	N	0.2
J0500.2+5237	0.21 ^{+0.17} _{-0.18}	1.4	228	bcu	GB6 J0500+5238	N	3.0
J0501.0+2424	1.27 ^{+0.85} _{-0.67}	3.8	43	bcu	1RXS J050107.1+242318	N	0.3
J0501.7+3048	0.49 ^{+0.30} _{-0.29}	3.4	99	bcu	GB6 J0501+3048	N	1.5
J0503.6+4518	0.31 ^{+0.45} _{-0.29}	1.1	51	bcu	GB6 J0503+4517	N	1.9
J0506.0+6113	0.91 ^{+0.38} _{-0.31}	17.6	141	bll	RX J0505.9+6113	N	2.7
J0515.8+1527	1.64 ^{+0.39} _{-0.34}	35.5	67	bll	GB6 J0515+1527	N	3.0
J0525.6-6013	1.31 ^{+0.34} _{-0.30}	28.7	85	bcu	SUMSS J052542-601341	N	0.8
J0526.7-1519	0.95 ^{+0.66} _{-0.47}	5.1	103	bcu	NVSS J052645-151900	N	0.9
J0532.0-4827	0.93 ^{+0.56} _{-0.67}	1.5	49	bll	PMN J0531-4827	N	0.5
J0540.5+5823	0.97 ^{+0.33} _{-0.25}	38.3	176	bll	GB6 J0540+5823	N	3.9
J0557.3-0615	0.61 ^{+0.69} _{-0.56}	1.2	45	bcu	1RXS J055717.0-061705	N	0.5
J0558.8-7459	1.74 ^{+0.87} _{-0.70}	6.3	59	bll	PKS 0600-749	N	0.0
J0600.3+1244	0.61 ^{+0.21} _{-0.16}	28.9	237	bcu	NVSS J060015+124344	N	4.8
J0601.0+3838	0.55 ^{+0.36} _{-0.26}	6.0	112	bll	B2 0557+38	N	3.1
J0601.3+5444	0.35 ^{+2.12} _{-0.18}	4.8	28	bcu	GB6 J0601+5443	N	0.3
J0607.4+4739	1.96 ^{+0.34} _{-0.34}	76.6	98	bll	TXS 0603+476	N	3.4
J0611.1+4325	1.53 ^{+0.50} _{-0.41}	21.5	40	bcu	7C 0607+4324	N	1.3
J0611.6-2712	1.19 ^{+1.63} _{-1.18}	1.0	-	bcu	PMN J0611-2709	N	0.1
J0612.8+4122	1.51 ^{+0.28} _{-0.25}	30.6	132	bll	B3 0609+413	N	5.5
J0617.2+5701	2.14 ^{+0.53} _{-0.42}	43.3	72	bll	87GB 061258.1+570222	N	1.6
J0623.2+3044	1.78 ^{+1.21} _{-0.73}	10.4	101	bll	GB6 J0623+3045	N	0.5
J0625.3+4439	1.44 ^{+0.60} _{-0.51}	8.4	106	bll	GB6 J0625+4440	N	0.9
J0629.6+2435	1.33 ^{+1.26} _{-1.07}	1.5	51	bcu	GB6 J0629+2437	N	0.2
J0647.0-5138	0.35 ^{+0.27} _{-0.21}	3.1	177	bcu	1ES 0646-515	N	2.4
J0700.2+1304	1.61 ^{+0.97} _{-0.66}	9.4	36	bll	GB6 J0700+1304	N	0.6
J0700.5-6610	1.53 ^{+0.33} _{-0.27}	40.8	146	bll	PKS 0700-661	N	0.9
J0702.7-1951	1.96 ^{+0.63} _{-0.49}	18.0	62	bll	TXS 0700-197	N	0.6
J0703.2+6809	0.89 ^{+1.03} _{-0.82}	1.2	62	bcu	GB6 J0703+6808	N	0.1
J0705.9+5309	0.77 ^{+0.77} _{-0.63}	1.6	13	bcu	GB6 J0706+5309	N	0.3
J0706.1+0246	0.49 ^{+0.26} _{-0.17}	13.1	470	bcu	1RXS J070609.7+024502	N	1.8
J0709.2-1527	0.81 ^{+0.28} _{-0.26}	16.6	127	bcu	PKS 0706-15	N	4.1
J0718.6-4319	0.77 ^{+0.51} _{-0.71}	1.1	75	bll	PMN J0718-4319	N	1.4
J0721.3-0222	1.07 ^{+0.70} _{-0.59}	2.8	42	bll	1RXS J072114.5-022047	N	0.4
J0723.0-0732	0.61 ^{+0.37} _{-0.34}	3.6	147	bll	1RXS J072259.5-073131	N	1.9
J0725.5+0216	0.99 ^{+0.69} _{-0.65}	2.1	44	bcu	NVSS J072534+021645	N	0.5
J0733.5-5445	1.72 ^{+1.26} _{-0.96}	2.9	15	bcu	SUMSS J073334-544544	N	0.0
J0737.3-8247	1.55 ^{+0.51} _{-0.44}	17.6	80	bcu	SUMSS J073706-824836	N	0.0
J0746.3-0225	0.79 ^{+0.56} _{-0.40}	6.1	85	bcu	2MASS J07462703-0225492	N	1.6
J0746.6-4754	0.89 ^{+0.23} _{-0.20}	25.1	103	bll	PMN J0746-4755	N	6.4
J0747.3-3310	1.38 ^{+0.88} _{-0.71}	3.6	44	bll	PKS 0745-330	N	0.3
J0747.5-4927	0.37 ^{+0.31} _{-0.27}	2.0	19	bcu	2MASS J07472476-4926332	N	2.5
J0749.0-2956	1.01 ^{+0.39} _{-0.30}	1.3	51	bcu	NVSS J074913-295658	N	0.1
J0754.0+0451	1.27 ^{+0.67} _{-0.55}	5.3	24	bcu	GB6 J0754+0452	N	0.6

4FGL Source Name (1)	Redshift Upper Limit (2)	TS_{peak} (3)	HEP (GeV) (4)	Type (5)	Association (6)	TeV (7)	CTA (σ) (8)
J0756.3–6431	$0.67^{+0.58}_{-0.51}$	1.8	40	bl	SUMSS J075625-643031	N	0.2
J0802.3–0942	$0.89^{+0.48}_{-0.39}$	6.4	68	bcu	NVSS J080216-094215	N	1.4
J0806.9–2151	$2.68^{+0.30}_{-1.64}$	5.4	24	bcu	TXS 0804-217	N	0.1
J0811.0–7529	$0.49^{+0.25}_{-0.18}$	1.9	94	bl	PMN J0810-7530	N	0.0
J0812.0+0237	$0.21^{+0.18}_{-0.15}$	2.0	149	bl	PMN J0811+0237	N	4.3
J0814.2–1013	$1.48^{+0.68}_{-0.57}$	8.5	79	bl	NVSS J081411-101208	N	0.7
J0826.4–6404	$0.17^{+0.20}_{-0.16}$	1.0	77	bl	SUMSS J082627-640414	N	4.3
J0829.6–1140	$1.86^{+0.81}_{-0.56}$	15.6	29	bcu	NVSS J082939-114103	N	0.4
J0829.7+5105	$1.03^{+0.64}_{-0.51}$	5.9	35	bl	GB6 J0829+5108	N	0.5
J0849.1+6607	$1.82^{+0.72}_{-0.53}$	19.7	–	bl	GB6 J0848+6605	N	0.8
J0849.4–2911	$1.44^{+1.04}_{-0.82}$	3.0	45	bcu	NVSS J084922-291149	N	0.1
J0853.1–3657	$0.93^{+0.29}_{-0.29}$	12.1	106	bcu	NVSS J085310-365820	N	3.2
J0856.4–5309	$1.38^{+0.30}_{-0.91}$	2.7	74	bcu	PMN J0856-5312	N	0.1
J0905.6+1358	$1.03^{+0.34}_{-0.33}$	11.5	125	bl	MG1 J090534+1358	N	3.8
J0929.3+5014	$0.45^{+0.47}_{-0.39}$	1.4	–	bl	GB6 J0929+5013	N	1.4
J0935.3–1736	$1.44^{+0.98}_{-0.62}$	9.1	–	bcu	NVSS J093514-173658	N	0.4
J0936.3–2111	$0.99^{+0.71}_{-0.95}$	1.0	–	bcu	TXS 0933-209	N	0.2
J0952.6–5048	$2.30^{+0.68}_{-1.64}$	3.2	–	bcu	2MASS J09524301-5049538	N	0.1
J0953.4–7659	$0.71^{+0.37}_{-0.31}$	8.1	101	bcu	RX J0953.1-7657	N	0.0
J1018.1+1905	$1.15^{+0.85}_{-0.72}$	2.1	34	bl	NVSS J101808+190614	N	0.3
J1022.4–4231	$1.53^{+1.43}_{-1.18}$	1.5	–	bl	PMN J1022-4232	N	0.0
J1027.0–8542	$2.10^{+0.29}_{-0.27}$	362.2	105	bl	PKS 1029-85	N	0.0
J1027.6+8251	$1.50^{+1.41}_{-0.94}$	2.8	50	bcu	2MASS J10284195+8253398	N	0.0
J1041.1–1201	$0.59^{+0.77}_{-0.42}$	2.3	59	bcu	NVSS J104108-120332	N	0.7
J1055.5–0125	$0.47^{+0.43}_{-0.39}$	1.5	107	bl	RX J1055.5-0126	N	1.4
J1107.6+0222	$2.06^{+0.74}_{-0.57}$	17.3	35	bl	NVSS J110735+022225	N	0.7
J1110.2+7135	$0.43^{+0.32}_{-0.28}$	2.5	65	bl	RX J1110.5+7133	N	1.5
J1123.8+7230	$0.53^{+0.38}_{-0.25}$	6.3	61	bl	RX J1123.8+7230	N	1.1
J1124.6–0809	$0.67^{+0.25}_{-0.66}$	1.1	29	bcu	AT20G J112437-080643	N	0.2
J1125.1–2101	$1.76^{+0.90}_{-0.62}$	12.6	50	bl	PMN J1125-2100	N	0.4
J1141.5–1408	$0.77^{+0.71}_{-0.54}$	2.3	23	bl	1RXS J114142.2-140757	N	0.5
J1155.5–3418	$0.81^{+0.48}_{-0.37}$	7.0	126	bcu	NVSS J115520-341718	N	1.4
J1156.6–2248	$1.44^{+0.99}_{-0.78}$	3.1	31	bcu	NVSS J115633-225004	N	0.1
J1220.1+3432	$1.35^{+1.11}_{-0.80}$	3.1	43	bl	GB2 1217+348	N	0.3
J1223.5+0818	$0.87^{+0.72}_{-0.60}$	2.2	39	bcu	SDSS J122327.49+082030.4	N	0.4
J1232.5–3720	$0.49^{+0.38}_{-0.34}$	2.2	52	bcu	NVSS J123235-372051	N	1.7
J1233.7–0144	$0.57^{+0.39}_{-0.37}$	2.3	79	bl	NVSS J123341-014426	N	1.7
J1240.1–6846	$1.50^{+1.50}_{-1.39}$	1.1	–	bcu	2MASS J12400694-6844532	N	0.0
J1240.4–7148	$0.65^{+0.33}_{-0.22}$	15.0	348	bcu	2MASS J12404205-7147599	N	2.9
J1248.3+5820	$2.68^{+0.18}_{-0.18}$	1672.9	198	bl	PG 1246+586	N	12.7
J1249.2–2809	$1.13^{+0.37}_{-0.52}$	5.4	29	bcu	GALEXASC J124926.84-280857.5	N	0.6
J1253.2+5301	$0.81^{+0.32}_{-0.32}$	5.8	155	bl	S4 1250+53	N	4.1
J1256.1–5919	$0.49^{+0.49}_{-0.45}$	1.2	52	bcu	PMN J1256-5919	N	0.5
J1259.8–3749	$0.75^{+0.51}_{-0.45}$	3.0	90	bl	NVSS J125949-374856	N	1.0
J1304.2–2412	$1.96^{+0.79}_{-0.57}$	17.1	34	bl	PMN J1304-2412	N	0.4
J1307.6–4259	$0.57^{+0.20}_{-0.17}$	13.4	114	bl	1RXS J130737.8-425940	N	9.2
J1311.8+3954	$1.25^{+1.19}_{-1.01}$	1.6	–	bl	FIRST J131146.0+395317	N	0.1
J1327.8+2522	$0.73^{+0.98}_{-0.66}$	1.3	12	bl	NVSS J132758+252750	N	0.2
J1328.5–4727	$0.77^{+0.36}_{-0.35}$	5.0	99	bl	1WGA J1328.6-4727	N	1.7
J1330.2+7002	$1.46^{+0.57}_{-0.48}$	11.0	49	bl	NVSS J133025+700141	N	0.6
J1338.9+1153	$0.75^{+0.84}_{-0.43}$	4.2	23	bl	SDSS J133859.05+115316.7	N	1.0
J1347.1–2959	$1.59^{+0.85}_{-0.82}$	9.4	56	bl	NVSS J134706-295840	N	0.3
J1349.5–7153	$0.67^{+0.83}_{-0.55}$	1.6	–	bcu	2MASS J13490974-7152510	N	0.1
J1351.3+1115	$1.31^{+0.42}_{-0.38}$	15.8	41	bl	RX J1351.3+1115	N	1.9
J1353.6–6640	$0.31^{+0.16}_{-0.17}$	3.5	127	bl	1RXS J135341.1-664002	N	5.6
J1406.1–2508	$0.87^{+0.78}_{-0.63}$	2.0	68	bl	NVSS J140609-250808	N	0.4
J1407.6–4301	$1.64^{+0.57}_{-0.92}$	2.9	18	bcu	SUMSS J140739-430231	N	0.1
J1411.5–0723	$0.33^{+1.05}_{-0.27}$	1.7	99	bcu	NVSS J141133-072252	N	0.7
J1420.3+0612	$0.93^{+1.41}_{-0.69}$	2.5	–	bl	SDSS J142013.69+061428.6	N	0.2
J1424.6+1447	$1.35^{+0.94}_{-0.66}$	4.9	–	bl	SDSS J142436.29+144910.5	N	0.4
J1427.7–3215	$0.85^{+0.56}_{-0.46}$	3.9	98	bl	NVSS J142750-321515	N	0.9

4FGL Source Name (1)	Redshift Upper Limit (2)	TS _{peak} (3)	HEP (GeV) (4)	Type (5)	Association (6)	TeV (7)	CTA (σ) (8)
J1432.2+5051	1.07 ^{+1.71} _{-0.95}	1.4	–	bcu	NVSS J143217+505603	N	0.1
J1434.8+6640	0.45 ^{+0.37} _{-0.41}	1.3	151	bil	1RXS J143442.0+664031	N	0.5
J1440.0–2343	0.81 ^{+0.48} _{-0.41}	4.4	22	bcu	PMN J1439-2341	N	1.1
J1446.8–1830	1.51 ^{+1.25} _{-0.91}	3.2	25	bcu	NVSS J144644-182922	N	0.1
J1448.0+3608	1.76 ^{+0.23} _{-0.20}	263.3	140	bil	RBS 1432	N	6.9
J1454.4+5124	1.29 ^{+0.26} _{-0.25}	22.4	78	bil	TXS 1452+516	N	4.3
J1455.8–7601	1.31 ^{+0.91} _{-0.75}	4.1	81	bcu	SUMSS J145543-760054	N	0.0
J1457.8–4642	0.71 ^{+0.39} _{-0.37}	5.2	55	bcu	PMN J1457-4642	N	0.6
J1511.8–0513	1.23 ^{+0.37} _{-0.34}	18.6	56	bil	NVSS J151148-051345	N	2.0
J1516.9+1934	2.88 ^{+0.10} _{-2.16}	1.7	–	bil	PKS 1514+197	N	0.1
J1518.0–2731	0.89 ^{+0.31} _{-0.31}	13.0	65	bil	TXS 1515-273	Y	4.2
J1520.0–0905	1.44 ^{+0.89} _{-0.65}	5.7	41	bcu	1RXS J151959.7-090434	N	0.2
J1528.2–2905	0.53 ^{+1.12} _{-0.49}	1.2	–	bcu	2MASS J15282165-2858132	N	0.2
J1532.7–1319	1.72 ^{+0.62} _{-0.56}	6.2	46	fsrq	TXS 1530-131	N	0.8
J1535.3–3135	1.82 ^{+1.15} _{-0.72}	11.0	–	bcu	2MASS J15352963-3133461	N	0.2
J1537.7–7957	1.70 ^{+0.88} _{-0.70}	5.2	34	bcu	PMN J1537-7958	N	0.0
J1537.9–1344	1.17 ^{+0.58} _{-0.46}	13.7	36	bcu	1RXS J153757.1-134334	N	0.8
J1539.7–1127	0.57 ^{+0.45} _{-0.41}	2.0	116	bil	PMN J1539-1128	N	1.6
J1549.8–0659	0.87 ^{+0.32} _{-0.30}	10.7	127	bcu	NVSS J154952-065907	N	2.9
J1553.5–3118	1.03 ^{+0.29} _{-0.28}	21.8	123	bil	1RXS J155333.4-311841	N	4.2
J1602.9–1928	1.17 ^{+1.35} _{-0.76}	3.1	15	bcu	2MASS J16024856-1929470	N	0.2
J1603.8–4903	0.17 ^{+0.13} _{-0.15}	1.2	133	bil	PMN J1603-4904	N	21.1
J1610.7–6648	1.46 ^{+0.14} _{-0.15}	125.8	124	bil	PMN J1610-6649	N	4.3
J1624.6+5651	1.27 ^{+1.15} _{-1.04}	1.4	24	bil	SBS 1623+569	N	0.1
J1632.2+0854	1.50 ^{+1.48} _{-1.01}	2.0	33	bcu	NVSS J163211+085608	N	0.1
J1637.7+7326	1.51 ^{+0.84} _{-0.52}	18.3	75	bil	RX J1637.9+7326	N	0.4
J1637.8–3449	1.33 ^{+0.35} _{-0.31}	27.4	64	bil	NVSS J163750-344915	N	2.6
J1646.7–1330	0.61 ^{+0.57} _{-0.50}	1.5	64	bcu	2MASS J16465897-1329454	N	0.6
J1647.4–6438	1.09 ^{+0.83} _{-0.64}	3.0	66	bcu	PMN J1647-6437	N	0.1
J1649.4+5235	1.94 ^{+0.68} _{-0.59}	7.7	61	bil	87GB 164812.2+524023	N	0.7
J1650.3–5045	1.96 ^{+0.67} _{-0.57}	13.0	67	bcu	PMN J1650-5044	N	0.5
J1651.6+7219	0.47 ^{+0.32} _{-0.31}	2.6	134	bil	RX J1651.6+7218	N	1.1
J1659.7–3131	0.85 ^{+0.76} _{-0.58}	2.8	18	bcu	NVSS J165949-313047	N	0.9
J1704.5–0527	0.41 ^{+0.25} _{-0.23}	3.4	165	bil	NVSS J170433-052839	N	4.5
J1735.4–1118	1.13 ^{+0.74} _{-0.82}	1.6	30	bcu	PMN J1735-1117	N	0.2
J1735.8–5932	0.83 ^{+0.82} _{-0.62}	1.9	60	bcu	1RXS J173553.1-593205	N	0.1
J1741.2+5739	1.13 ^{+1.23} _{-0.95}	1.4	–	bcu	NVSS J174111+573812	N	0.1
J1744.4+1851	0.91 ^{+0.64} _{-0.41}	11.6	100	bcu	1RXS J174420.1+185215	N	0.8
J1744.6–5713	1.78 ^{+0.79} _{-0.57}	15.1	41	bil	PMN J1744-5715	N	0.1
J1744.9–1727	0.21 ^{+0.17} _{-0.16}	1.8	197	bcu	1RXS J174459.5-172640	N	8.5
J1748.1+2702	1.25 ^{+1.07} _{-1.08}	1.3	31	bcu	87GB 174618.6+270457	N	0.1
J1759.1–4822	1.40 ^{+1.24} _{-1.33}	1.0	15	bcu	PMN J1758-4820	N	0.0
J1800.1+2812	1.40 ^{+1.04} _{-1.06}	1.6	37	bcu	NVSS J180002+281050	N	0.1
J1800.1+7037	1.53 ^{+0.95} _{-0.68}	6.4	56	bil	RX J1759.8+7037	N	0.3
J1809.7+2910	1.42 ^{+0.48} _{-0.44}	10.6	62	bil	MG2 J180948+2910	N	1.6
J1810.7+5335	2.02 ^{+0.88} _{-0.64}	12.7	19	bcu	2MASS J18103800+5335016	N	0.3
J1811.0+1608	0.63 ^{+1.16} _{-0.62}	1.0	10	bil	87GB 180835.5+160714	N	0.4
J1820.3+3624	1.40 ^{+0.84} _{-1.15}	3.4	55	bil	NVSS J182021+362343	N	0.4
J1823.6–3453	0.29 ^{+0.12} _{-0.12}	7.0	177	bcu	NVSS J182338-345412	N	23.9
J1829.3+5402	1.38 ^{+0.54} _{-0.38}	20.2	66	bil	RX J1829.3+5403	N	1.2
J1830.0+1324	1.50 ^{+0.90} _{-0.74}	4.0	55	bil	MG1 J183001+1323	N	0.4
J1832.6–5658	1.05 ^{+1.39} _{-0.74}	3.3	41	bil	PMN J1832-5659	N	0.1
J1841.3+2909	0.27 ^{+0.28} _{-0.23}	1.4	58	bil	MG3 J184126+2910	N	2.2
J1844.4+1547	0.93 ^{+0.35} _{-0.34}	7.4	162	bil	NVSS J184425+154646	N	3.8
J1845.0+1613	0.99 ^{+0.85} _{-0.87}	1.3	16	bcu	87GB 184225.9+161105	N	0.3
J1846.7+7238	1.13 ^{+0.71} _{-0.58}	4.1	42	bcu	RX J1846.1+7237	N	0.3
J1850.5+2631	0.83 ^{+0.32} _{-0.26}	20.7	138	bil	NVSS J185023+263151	N	1.9
J1858.5+0640	1.25 ^{+0.77} _{-0.86}	2.8	54	bcu	NVSS J185831+064016	N	0.8
J1859.0+2329	0.63 ^{+0.81} _{-0.62}	1.0	–	bcu	NVSS J185857+233007	N	0.4
J1903.2+5540	0.83 ^{+0.21} _{-0.27}	11.2	144	bil	TXS 1902+556	N	7.1
J1909.5+3511	2.92 ^{+0.04} _{-1.25}	15.9	57	bcu	TXS 1907+350	N	0.2

4FGL Source Name (1)	Redshift Upper Limit (2)	TS _{peak} (3)	HEP (GeV) (4)	Type (5)	Association (6)	TeV (7)	CTA (σ) (8)
J1912.1–0803	0.87 ^{+0.74} _{-0.72}	1.4	75	bcu	PMN J1912-0804	N	0.4
J1913.9+4439	1.94 ^{+0.87} _{-0.66}	5.6	34	bil	1RXS J191401.9+443849	N	0.4
J1918.1+3752	0.91 ^{+0.81} _{-0.73}	1.6	54	bcu	1RXS J191810.2+375315	N	0.3
J1921.3–1231	1.72 ^{+0.65} _{-0.54}	11.1	63	bil	TXS 1918-126	N	0.5
J1925.0+2815	0.39 ^{+0.38} _{-0.28}	2.2	46	bcu	NVSS J192502+281542	N	2.0
J1925.8–2220	0.43 ^{+0.46} _{-0.40}	1.2	104	bil	TXS 1922-224	N	1.0
J1926.8+6154	1.17 ^{+0.18} _{-0.19}	81.8	78	bil	87GB 192614.4+614823	N	6.7
J1927.5+6117	1.29 ^{+0.48} _{-0.40}	12.5	61	bil	S4 1926+61	N	1.2
J1933.3+0726	0.61 ^{+0.30} _{-0.18}	20.8	189	bil	1RXS J193320.3+072616	N	7.7
J1942.5–5827	0.77 ^{+0.86} _{-0.75}	1.1	–	bcu	SUMSS J194224-582824	N	0.1
J1942.7+1033	0.55 ^{+0.12} _{-0.12}	35.6	180	bil	87GB 194024.3+102612	N	18.5
J1944.4–4523	0.61 ^{+0.32} _{-0.27}	6.5	50	bcu	1RXS J194422.6-452326	N	2.4
J1946.0+0937	1.46 ^{+0.72} _{-0.55}	12.3	97	bcu	87GB 194328.9+092856	N	0.7
J1949.5+0906	1.31 ^{+0.32} _{-0.43}	12.9	50	bil	1RXS J194934.1+090655	N	1.3
J1955.1–1604	1.13 ^{+0.43} _{-0.38}	13.3	40	bil	1RXS J195500.6-160328	N	1.6
J2001.2+4353	2.48 ^{+0.30} _{-0.33}	336.4	155	bil	MG4 J200112+4352	Y	5.5
J2002.4–7119	0.53 ^{+0.32} _{-0.27}	4.6	113	bcu	SUMSS J200227-711940	N	1.3
J2002.6+6302	1.90 ^{+0.68} _{-0.52}	30.5	98	bcu	1RXS J200245.4+630226	N	0.5
J2005.1+7003	0.95 ^{+0.42} _{-0.45}	2.9	77	bil	1RXS J200504.0+700445	N	1.6
J2012.0+4629	0.81 ^{+0.21} _{-0.21}	12.5	89	bil	7C 2010+4619	N	8.6
J2024.4–0847	0.51 ^{+0.49} _{-0.47}	1.2	28	bil	1RXS J202428.9-084810	N	1.1
J2025.3–2231	0.55 ^{+0.57} _{-0.42}	1.8	62	bcu	NVSS J202515-223016	N	1.0
J2026.1+7645	0.51 ^{+0.23} _{-0.20}	11.0	192	bcu	1RXS J202633.4+764432	N	2.7
J2026.6+3449	1.57 ^{+0.78} _{-0.62}	9.2	28	bcu	NVSS J202638+345022	N	0.8
J2035.9+4901	0.63 ^{+0.45} _{-0.43}	2.2	99	bcu	2MASS J20355146+4901490	N	1.1
J2039.0–1046	0.99 ^{+0.62} _{-0.89}	1.1	38	bil	TXS 2036-109	N	0.3
J2040.1–4621	1.13 ^{+0.81} _{-0.59}	5.3	37	bcu	2MASS J20400660-4620180	N	0.4
J2041.8–7319	1.57 ^{+0.64} _{-0.51}	13.4	52	bcu	SUMSS J204201-731911	N	0.1
J2045.1–2346	1.09 ^{+0.71} _{-0.50}	7.4	13	bcu	NVSS J204457-234643	N	0.6
J2047.9–3122	1.03 ^{+1.02} _{-0.77}	1.8	–	bcu	NVSS J204806-312016	N	0.2
J2056.7+4939	0.17 ^{+0.06} _{-0.07}	6.4	309	bcu	RGB J2056+496	Y	18.7
J2102.3+4702	1.42 ^{+0.64} _{-0.57}	5.4	54	bcu	MG4 J210218+4702	N	0.7
J2104.3–0212	0.75 ^{+0.36} _{-0.26}	19.5	113	bil	NVSS J210421-021239	N	3.3
J2108.9–6638	1.78 ^{+0.76} _{-0.58}	8.6	57	bil	PKS 2104-668	N	0.1
J2109.8–8618	0.33 ^{+0.35} _{-0.32}	1.1	88	bcu	1RXS J210959.5-861853	N	0.0
J2110.3+0404	1.27 ^{+1.39} _{-1.22}	1.1	24	bcu	NVSS J211019+040418	N	0.1
J2115.2+1218	0.57 ^{+0.45} _{-0.43}	1.9	119	bcu	NVSS J211522+121802	N	0.9
J2126.1–3922	0.97 ^{+1.04} _{-0.80}	1.7	–	bcu	PMN J2126-3921	N	0.2
J2126.5+1842	1.05 ^{+0.87} _{-0.77}	3.0	–	bcu	87GB 212407.5+182753	N	0.5
J2127.7+3612	0.53 ^{+0.45} _{-0.47}	1.2	37	bil	B2 2125+35	N	1.8
J2133.9+6646	2.26 ^{+0.97} _{-0.55}	30.1	65	bil	NVSS J213349+664706	N	0.8
J2139.4–4235	1.96 ^{+0.22} _{-0.23}	206.2	152	bil	MH 2136-428	N	6.1
J2142.1+4501	1.53 ^{+1.21} _{-0.88}	4.2	–	bcu	B3 2140+447	N	0.2
J2142.4+3659	0.77 ^{+0.42} _{-0.36}	5.7	25	bcu	2MASS J21422658+3659481	N	1.1
J2144.2+3132	0.79 ^{+0.78} _{-0.74}	1.1	85	bil	MG3 J214415+3132	N	0.4
J2156.0+1818	0.79 ^{+0.34} _{-0.30}	12.5	215	bil	RX J2156.0+1818	N	2.7
J2210.8+3203	0.51 ^{+0.35} _{-0.23}	7.9	347	bcu	1RXS J221058.3+320327	N	0.8
J2213.5–4754	1.53 ^{+0.95} _{-0.76}	4.8	28	bcu	SUMSS J221330-475426	N	0.2
J2215.4+0544	1.40 ^{+1.16} _{-0.91}	2.4	–	bcu	NVSS J221513+054454	N	0.2
J2229.1+2254	1.82 ^{+1.15} _{-0.73}	11.2	49	bcu	NVSS J222913+225511	N	0.2
J2247.8+4413	0.37 ^{+0.17} _{-0.15}	7.0	169	bil	RGB J2247+442	N	4.6
J2300.3+3136	1.68 ^{+0.79} _{-0.74}	3.2	45	bil	NVSS J230022+313703	N	0.8
J2300.8–0736	0.35 ^{+0.40} _{-0.31}	1.3	157	bcu	2MASS J23005469-0735438	N	1.3
J2304.6+3704	0.93 ^{+0.28} _{-0.25}	21.5	153	bil	1RXS J230437.1+370506	N	3.3
J2313.4–6922	1.50 ^{+0.81} _{-0.57}	14.3	17	bcu	SUMSS J231347-692332	N	0.1
J2321.7–6438	0.71 ^{+0.46} _{-0.47}	2.2	53	bcu	PMN J2321-6438	N	0.3
J2329.7+6101	0.65 ^{+0.32} _{-0.27}	7.1	143	bcu	NVSS J232938+610113	N	2.5
J2339.2–7403	0.43 ^{+0.46} _{-0.40}	1.2	86	bcu	1RXS J233919.8-740439	N	0.6
J2351.3–7559	0.77 ^{+0.35} _{-0.45}	3.7	134	bil	SUMSS J235115-760012	N	0.0

Table 1. Column information are as follows: (1) 4FGL source name; (2) redshift upper limit, i.e., the redshift at TS_{peak} derived from our EBL-attenuation methodology, uncertainties are at 68% C.L.; (3) value of the peak of the Test Statistic profile; (4) highest energy photon; (5) source type (bil is BL Lac and bcu is blazar candidate of uncertain type); (6) source association; (7) whether the source is detected by IACTs, Yes or No; (8) predicted significance of CTA detection in 20h, either from CTA-North (positive declination) or CTA-South (negative declination) depending on the observability of the source. *MNRAS* **000**, 1–8 (2022)